Measurement of the ^{17} O(p,γ)^{18}F reaction rate at astrophysically relevant energies

U. Hager, L. Buchmann, B. Davids, J. Fallis, B. R. Fulton, N. Galinski, U. Greife, D. A. Hutcheon, D. Ottewell, A. Rojas, C. Ruiz, and K. Setoodehnia

Phys. Rev. C **85**, 035803 — Published 14 March 2012

DOI: 10.1103/PhysRevC.85.035803

Measurement of the $^{17}O(p,\gamma)^{18}F$ reaction rate at astrophysically relevant energies

U. Hager,[1,*] L. Buchmann,[2] B. Davids,[2] J. Fallis,[2] B.R. Fulton,[3] N. Galinski,[2]
U. Greife,[1] D. A. Hutcheon,[2] D. Ottewell,[2] A. Rojas,[2] C. Ruiz,[2] and K. Setoodehnia[4]

[1] *Colorado School of Mines, Golden, CO, USA*
[2] *TRIUMF, Vancouver, Canada V6T 2A3*
[3] *Department of Physics, University of York, York, YO10 5DD, UK*
[4] *McMaster University, Hamilton, ON, Canada*

The $^{17}O(p,\gamma)^{18}F$ reaction plays a important role in hydrogen burning nucleosynthesis. Conflicting values for the low-energy behavior of its cross section exist in the literature. We present direct measurements of the astrophysical S factor of the $^{17}O(p,\gamma)^{18}F$ reaction at center-of-mass energies between 250 and 500 keV. These measurements were conducted in inverse kinematics at the DRAGON recoil separator.

PACS numbers: 26.30.-k,26.50.+x,98.80.Ft,24.50.+g,25.40.Lw

I. INTRODUCTION

One of the goals of satellite-based γ-astronomy is to observe the emission of 511 keV γ radiation from classical novae. This emission is produced by electron-positron annihilation following the β^+ decay of radioactive nuclei in the expanding envelope [1]. ^{18}F is expected to be the most important contributor, since due to a half-life of 110 min, it is still undergoing β-decay when the envelope becomes transparent to γ-rays.

^{18}F nucleosynthesis in classical novae strongly depends on the thermonuclear rate of $^{17}O(p,\gamma)^{18}F$ [2], which is part of the hot CNO cycle (Fig. 1) [3]; The relevant temperature range is between 0.1 and 0.4 GK [4]. The location of the corresponding Gamow windows with respect to the level structure of ^{18}F is shown in Fig. 2. Using a hydrodynamic nova model with a nuclear reaction network, José *et al.* [5] predict that ^{17}O is among the main products in the ejecta of classical novae.

The amount of ^{18}F produced depends on the ratio of the $^{17}O(p,\gamma)^{18}F$ and $^{17}O(p,\alpha)^{14}N$ rates. Iliadis *et al.* [6] used temperature-density-time profiles from hydrodynamic nova simulations and varied the reaction rates within their estimated uncertainties. They found that the ^{18}F abundance was sensitive to the reaction rate uncertainties at that time, with variations of up to a factor 100 in abundance for variations of the rates of $^{18}F(p,\alpha)^{15}O$, $^{17}O(p,\alpha)^{14}N$ and $^{17}O(p,\gamma)^{18}F$ within their uncertainties.

At astrophysically relevant temperatures, resonances and direct capture both contribute to the reaction rate.

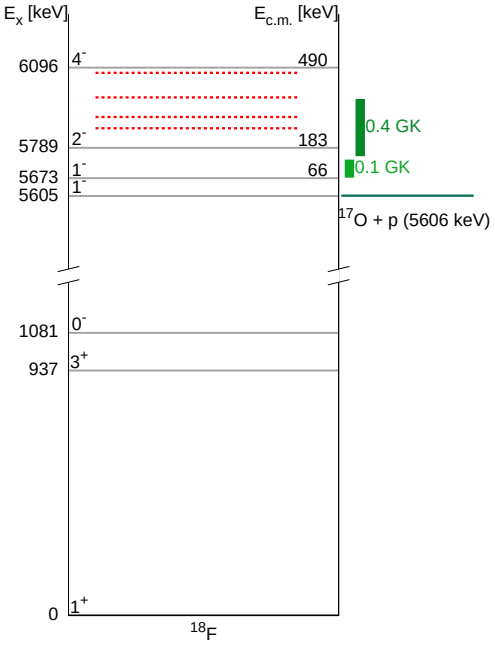

FIG. 2. (color online) Levels in ^{18}F. On the right hand side, Gamow windows corresponding to 0.1 GK and 0.4 GK are indicated. The red, dashed lines represent the energies discussed in the present work.

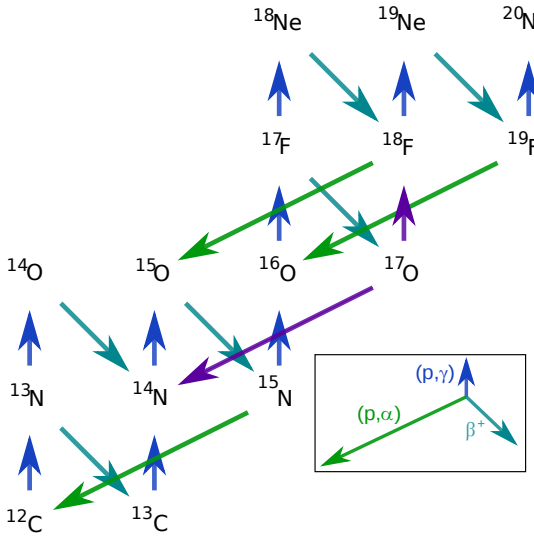

FIG. 1. (color online) The hot CNO cycle.

* uhager@mines.edu

Below $T = 0.03$ GK, direct capture (DC) accounts for almost 90% of the total rate. For $T = 0.09 - 0.55$ GK ($E_{\rm c.m.} \approx 100 - 250$ keV) the DC process dominates the total reaction rate with the $E_{\rm c.m.} = 183$ keV resonance contributing less than 40%. At higher temperatures, the DC contribution decreases and the reaction proceeds mainly through higher-lying resonances [4]. The literature on ^{17}O$(p,\gamma)^{18}$F gives conflicting information for the DC component of the reaction rate.

Rolfs [7] measured the cross section using anodized ^{17}O targets on tantalum and tungsten backings by measuring prompt γ-rays from the reaction. The reaction was assumed to proceed exclusively via DC at nova temperatures, and the S factor was extracted to be constant at $S_{DC} \approx 9$ keVb for $E_{\rm c.m.} = 100 - 500$ keV. Fox *et al.* [4] used Ta_2O_5 targets at TUNL with proton beams of up to 100 μA in the energy range $E_p^{lab} = 180 - 540$ keV ($E_{\rm c.m.} = 170 - 470$ keV). γ-rays from the reaction were detected using a large-volume high-purity germanium detector. Spectroscopic factors of 21 levels in ^{18}F were used to calculate the direct capture S factor as $S_{DC} = 3.74 + 0.676E_{\rm c.m.} - 0.249E_{\rm c.m.}^2$ keVb, and to determine the influence of higher-lying resonances on the total S factor at astrophysically relevant energies. Chafa *et al.* [2] used an activation method to determine the DC S factor. ^{17}O targets were irradiated, and the subsequent β^+ decay of the produced ^{18}F was measured via coincidences of the 511 keV γ-rays from positron-electron pair annihilation. They determined $S_{DC} = 8.3 \pm 4.0$ keVb at $E_{\rm c.m.} = 180.2$ keV, and calculated $S_{DC} = 6.2 + 1.61E_{\rm c.m.} - 0.169E_{\rm c.m.}^2$ keVb. This DC S factor is larger than the one found in Ref. [4] by more than 50%. The discrepancy might be due to the use of the activation method in Ref. [2], which measures the integral yield regardless of which γ transitions were involved, rather than measuring prompt γ-rays as in Ref. [4], in which case some transitions might not be observed. On the other hand, some of the measured 511 keV γ-rays might come from different sources, although care was taken to disentangle the different contributions. The resulting rates given in Refs. [2, 4] differ by approximately a factor 2; a larger reaction rate would translate almost linearly into an increase of the final abundances of ^{18}O, ^{18}F, and ^{19}F.

Recently, Newton *et al.* [8] measured the direct capture cross section below the narrow resonance at $E_{\rm c.m.} = 494$ keV using implanted ^{17}O targets at TUNL, similar to the measurement by Fox *et al.* [4]. They recommend an S factor of $S_{DC} = 4.6$ keVb ($\pm$23%) below $E_{\rm c.m.} = 500$ keV.

The experiments described here aim at clarifying the energy dependence of the S factor above the $E_{\rm c.m.} = 183$ keV resonance which in previous publications had been described as either constant [7] or decreasing with energy [4, 8]. This low energy behavior is an important factor in the overall calculation of astrophysical reaction rates.

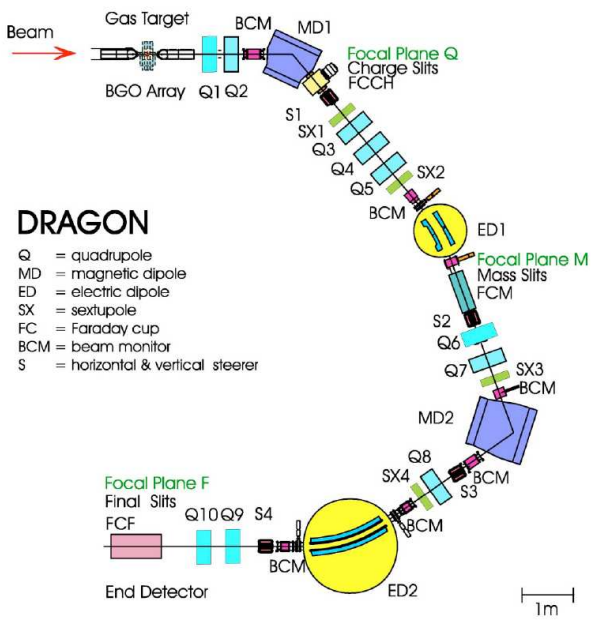

FIG. 3. (color online) Schematic view of the DRAGON facility.

TABLE I. Beam energies covered by the gas target and corresponding center-of-mass energies and excitation energies in ^{18}F.

$E_{\rm beam}$[AkeV]	$E_{\rm c.m.}$[MeV]	$E_{\rm x}$[MeV]
505 – 482.5	0.481 – 0.459	6.087 – 6.065
407.0 – 384.5	0.387 – 0.366	5.993 – 5.972
327.0 – 304.0	0.311 – 0.289	5.918 – 5.896
282.9 – 259.5	0.269 – 0.247	5.875 – 5.853

II. EXPERIMENTAL PROCEDURE

The measurements were performed in inverse kinematics at the DRAGON recoil separator [9], located at the ISAC facility at TRIUMF, Vancouver, Canada. A schematic view of the DRAGON facility is shown in Fig. 3. The stable ^{17}O beam was produced by the Supernanogan off-line ECR ion source [10]. The beam intensity on target was initially $0.5 \cdot 10^{12}$ s^{-1} and increased to $\approx 1.5 \cdot 10^{12}$ s^{-1} during the course of the experiment. The DRAGON windowless gas target was filled with hydrogen maintained at a pressure within 3% of 7 Torr (measurement uncertainty of 2%), with an effective target length of 12.3 ± 0.4 cm [9]. Table I lists the beam energies studied in this work, the energy ranges covered by the target, and the center-of-mass energy at the center of the target. Due to the limited beam time available, these energies were chosen to provide adequate yields while still reaching the astrophysically relevant energy region, and to be able to compare with data presented by Rolfs [7] and Newton *et al.* [8]. Several charge states were measured for each energy, as described in Section III C below.

A. Beam normalization

The normalization procedure outlined in Ref. [11] was followed to determine the integrated beam current on target. The target housed two surface barrier silicon detectors at 30° and 57° to the beam axis to monitor scattered protons for beam normalization. In addition, regular measurements with a Faraday cup upstream of the target were taken to relate the beam current to the scattering inside the target. The reaction rate measurements at each energy and charge state were split into multiple runs of about 55 min duration. Before and after each run measurements of the beam current on the Faraday cup were taken. The current was recorded and averaged over an interval of 30 s to minimize the impact of short term fluctuations. The two current readings were then compared to the rate of elastic scattering in the target onto the 30° detector during the first and last minute of the measurement run, respectively, thus minimizing the time between current and scattering measurements. The normalization factor R was determined using the relation

$$R = \frac{I/q}{e}\frac{\Delta t}{N_p}\frac{P}{E^2_{\rm beam}}\epsilon_{\rm target} \qquad (1)$$

where I is the beam current measured on the Faraday cup, q is the charge state of the beam, e is the elementary charge, Δt is the time window during which the scattered protons were counted (*i.e.* 60 s), N_p is the number of protons scattered onto the detector during Δt, P is the target pressure in torr, and $E_{\rm beam}$ is the beam energy in AkeV. $\epsilon_{\rm target}$ is the transmission through the target, measured with an empty target, and limited mainly by the target entrance aperture. The factor $\frac{P}{E^2_{\rm beam}}$ describes Rutherford scattering, and was intended to make the normalization independent of the beam energy and the target pressure. It was, however, found that this correction was insufficient, and the normalization was performed separately for each energy. The normalization factor R was thus determined for every run, giving two values of R per run. All those individual normalization factors were then averaged for each measured energy. Figure 4 shows the normalization factor R for the measurement at $E_{\rm c.m.} = 300\,$keV and charge state 4^+. In order to determine the total beam on target, the number of elastically scattered protons was integrated for all runs at one energy and charge state. Since no background was observed in the elastic scattering monitor, the square-root of the counts was used as the uncertainty of the value.

The number of ^{17}O ions on target for each energy and recoil charge state is given in Table II.

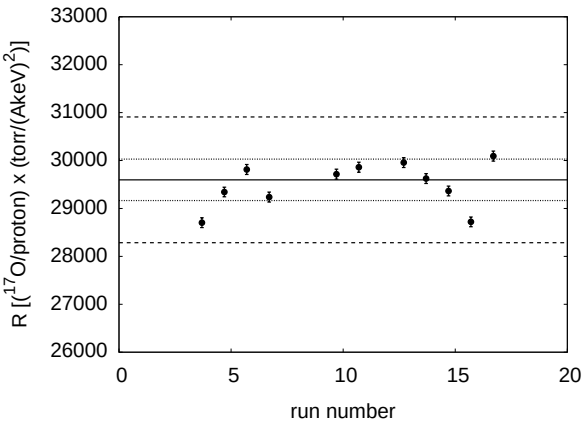

FIG. 4. Normalization factor R with statistical uncertainties for the measurements at $E_{\rm c.m.} = 300\,$keV in charge state 4^+. The solid line represents the average, the dotted line its statistical and the dashed lines its total uncertainty.

B. Recoil detection

The DRAGON target was surrounded by an array of 30 BGO (bismuth germanate) γ-detectors in a tight geometry. The detectors were calibrated using the 6.13 MeV γ-ray emitted by a ^{244}Cm-^{13}C source and adjusting their high-voltage PMT biases until the source peak lined up in all detectors. Given the resolution of the BGO array (about 20% at 660 keV for the whole array), this calibration with the assumption of linearity is sufficient for the purpose of this work. The ^{18}F ions produced in the reaction were detected in the separator's focal plane in coincidence with γ events in the BGO array, after separation from the beam using a two-stage electromagnetic separator with an angular acceptance of 21 mrad. The maximum cone angles of the recoils in this work varied between 12 mrad for $E_{\rm c.m.} = 470\,$keV and 15 mrad for $E_{\rm c.m.} = 258\,$keV. These angles are calculated assuming decay of the reaction product directly to the ground state emitting a single γ-ray. For decay through a cascade, the average cone angle will decrease and the effect of the angular acceptance on the recoil detection efficiency has to be determined from simulations, see Section III B.

At the focal plane of the separator, the recoils were detected either in an ionization chamber (IC) [12] or a double-sided silicon strip detector (DSSSD). The IC had a segmented anode to provide $\Delta E - E$ information, and thus particle identification. The DSSSD, apart from the energy E, provided position information and faster timing. For the two highest energies, $E_{\rm c.m.} = 470\,$keV and $E_{\rm c.m.} = 377\,$keV, the IC was used. For the two lowest energies, the DSSSD was the better choice because the signal in the IC became too small to provide reliable particle identification. At $E_{\rm c.m.} = 300\,$keV, measurements with both detectors were taken.

Upstream of the focal plane detectors, a local time-of-flight (TOF) setup was situated [13] consisting of

TABLE II. Integrated ^{17}O beam on target for each measured beam energy and recoil charge state. The statistical and systematic uncertainties are given separately.

	charge state			
$E_{\mathrm{c.m.}}$	3^+	4^+	5^+	6^+
470			$(6.95 \pm 0.004 \pm 0.41) \times 10^{15}$	$(1.83 \pm 0.0006 \pm 0.11) \times 10^{16}$
377		$(1.49 \pm 0.0005 \pm 0.11) \times 10^{16}$	$(3.75 \pm 0.002 \pm 0.26) \times 10^{15}$	$(3.79 \pm 0.003 \pm 0.26) \times 10^{15}$
300	$(2.13 \pm 0.0004 \pm 0.13) \times 10^{16}$	$(5.12 \pm 0.002 \pm 0.31) \times 10^{15}$	$(4.93 \pm 0.002 \pm 0.29) \times 10^{15}$	$(4.64 \pm 0.002 \pm 0.28) \times 10^{15}$
258	$(1.02 \pm 0.0004 \pm 0.06) \times 10^{17}$	$(1.11 \pm 0.0004 \pm 0.06) \times 10^{17}$	$(1.77 \pm 0.0004 \pm 0.10) \times 10^{17}$	

two MCPs (micro-channel plates) separated by approximately 60 cm flight path. This system provided good resolution even at low energies, where the separator background suppression decreases [14]. The MCP system is operated in such a way that the signal from the second MCP is used as the start signal for a time-to-analog converter (TAC), and the delayed signal from the first MCP provides the stop for the TAC. The delay of the stop signal is adjusted to accommodate the input range of the ADC. In coincidence with a γ event in the BGOs, the MCP timing signal also improved the time-of-flight measurement through the separator.
From the measured yield Y the cross-section σ can be derived using [3]

$$Y = \sigma n \Delta x \ , \tag{2}$$

where n is the target density, and Δx the target thickness. The S factor is defined as

$$\sigma(E) = S(E)\frac{1}{E}e^{-2\pi\eta} \ , \tag{3}$$

where η is the Sommerfeld parameter.

III. ANALYSIS AND RESULTS

A. Particle identification

As mentioned above, the data was taken partly using the IC, and partly using the DSSSD. While it had been intended to take advantage of the $\Delta E - E$ information provided by the IC, neither it nor the DSSSD was used for particle identification (PID). In order to use a consistent PID for all runs, both detectors were instead used to determine the efficiency of the MCP TOF system. At $E_{\mathrm{c.m.}} = 300$ keV, where measurements were performed with both detectors, the efficiency of the MCPs in coincidence was found to be 84(6)% using the DSSSD and 82(6)% using the IC. The MCP efficiency was determined for each energy, and the weighted average was found to be 86(5)%. The times-of-flight through the separator and between the MCPs were used to identify recoil events. Figure 5 shows an example spectrum of the time-of-flight through the separator, and Fig. 6 shows a MCP time-of-flight spectrum. Both show data taken during the measurement at $E_{\mathrm{c.m.}} = 258$ keV and recoil charge state 4^+, illustrating the DRAGON's suppression capabilities even at this low energy. The total number of recoils that were thus identified at each energy and charge state are given in Table III.

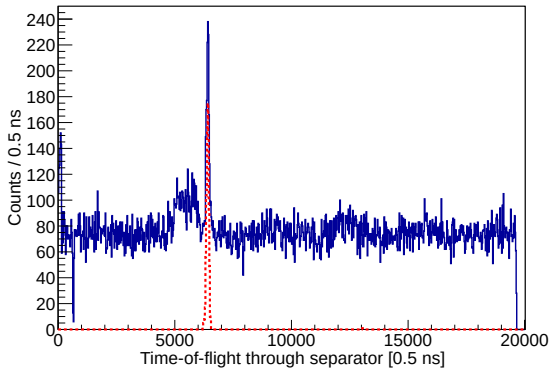

FIG. 5. (color online) Time-of-flight through the separator for $E_{\mathrm{c.m.}} = 258$ keV and recoil charge state 4^+. The solid, blue line represents all coincidence events; the events that passed software cuts on both MCP and separator time-of-flight are shown in red (dashed line).

TABLE III. Coincident recoil events for each measured energy and charge state.

	charge state			
$E_{\mathrm{c.m.}}$	3^+	4^+	5^+	6^+
470		4697	2209	
377		1327	516	218
300	208	141	78	6
258	518	939	487	

B. Simulations and branching ratios

The opening angle of a reaction at a given energy depends on the number of γ-rays emitted as the product deexcites to the ground state. This affects the efficiency of the separator. Similarly, the probability of detecting an event in the BGO array depends on the number of emitted γs and their energies. Therefore, the branching ratio into different cascades had to be determined. To this end, separate GEANT3 simulations were conducted for capture

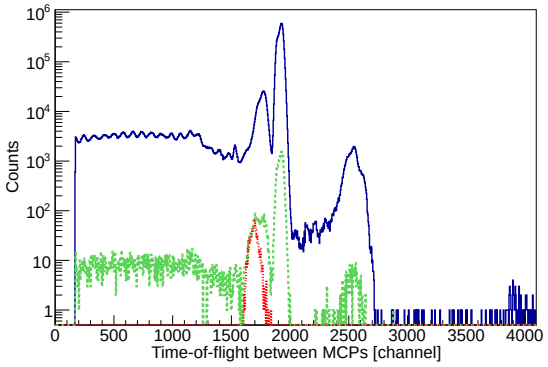

FIG. 6. (color online) Time-of-flight between the MCPs for $E_{\mathrm{c.m.}} = 258\,\mathrm{keV}$ and recoil charge state 4^+. Higher channels correspond to a shorter time-of-flight, and thus higher velocity. The solid, blue line represents all single events; the green, dashed line represents all coincidence events; the coincidence events that passed software cuts on both MCP and separator time-of-flight are represented by the red, dotted line. The additional peaks are due to 'leaky' ^{17}O beam. The 'leaky' beam can have a range of different energies, since it must scatter at least once in the separator in order to be transmitted to the MCPs. The abscissa represents the output amplitude of the TAC.

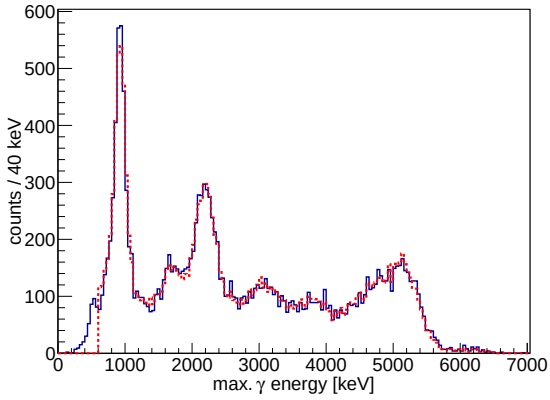

FIG. 7. (color online) BGO γ spectrum taken at $E_{\mathrm{c.m.}} = 470\,\mathrm{keV}$. The solid, blue line is the data, the dashed, red line is the fit including transitions to excited states at 937, 2523, 3062, 3791, 3839, 4116, 4398, and 4964 keV.

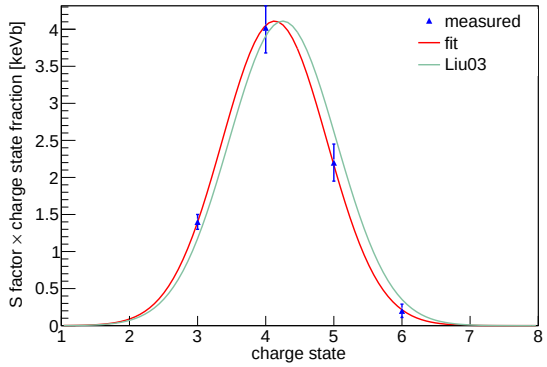

FIG. 8. (color online) S factor $\times$ charge state fraction for charge states $3^+, 4^+, 5^+, 6^+$ at $E_{\mathrm{c.m.}} = 300\,\mathrm{keV}$, measured values are in blue, the Gaussian fit in red, and the calculation from Ref. [17] normalized to the measured values are shown in green.

into different states. Similar simulations have been found to reproduce both the geometric efficiency of the array as a whole and the intrinsic efficiency of the individual BGO detectors very well [15]. The branching ratios of the subsequent decay cascades were taken from Tilley *et al.* [16]. For each cascade 10000 events were simulated. The resulting simulated γ spectra were fitted to the measured ones. This was done within the ROOT data analysis framework using the `TFractionFitter` class which uses Poisson statistics to take into account statistical uncertainties both in the data and the simulation. An example of such a fit is shown in Fig. 7 for the measurement at $E_{\mathrm{c.m.}} = 470\,\mathrm{keV}$. To improve statistics, the data for all charge states were summed, as the branching ratios do not depend on the measured charge state. Table IV lists the branching ratios for each energy, and the resulting BGO efficiency at this energy. For the lowest energy point at $E_{\mathrm{c.m.}} = 258\,\mathrm{keV}$, it was not possible to distinguish decay through the 937 keV state (emitted γ-rays: 4927 keV and 937 keV) from decay through the 4964 keV state (900 keV and 4964 keV γ-rays). However, as Table IV shows, the 4964 keV state does not contribute at the other measured energies, and its branching ratio was therefore assumed to be 0.

Together with the uncertainty in the beam on target, the resulting uncertainty in the BGO efficiency is the dominant uncertainty in the experiment.

The separator transmission was determined for each energy in the same way. It was 96(7)% for $E_{\mathrm{c.m.}} = 258\,\mathrm{keV}$, 97(3)% for $E_{\mathrm{c.m.}} = 300\,\mathrm{keV}$, and 98(2)% for the two highest energies.

C. Charge state distributions

Since the recoils exit the target in a distribution of charge states, but the separator only transmits one charge state at a time, it is important to know what the charge state distribution after the DRAGON target looks like. Liu *et al.* [17] studied this distribution and derived semi-empirical equations characterizing it.

In the present work, several charge states were studied for each energy. Since the charge state ratios were unknown, the S factor strength in each charge state was calculated using Eq. 3 for each charge state separately. For each energy, the resulting contributions to the S factor in each charge state as a function of charge state was fitted following Ref. [17] using a Gaussian distribution. As an example, the distribution for $E_{\mathrm{c.m.}} = 300\,\mathrm{keV}$ is shown in Fig. 8. Also shown is the calculated distribution from Ref. [17].

Since only two charge states were measured for the high-

TABLE IV. Branching ratios (BR) and BGO efficiencies for each measured energy. No entry means this transition was not included in the fit.

	BR for DC to level at [keV]									
$E_{\mathrm{c.m.}}$ [keV]	937	1121	2523	3062	3791	3839	4116	4398	4964	BGO efficiency
470	0.493(14)	< 0.003	0.033(22)	0.020(2)	0.044(34)	0.304(39)	0.043(20)	0.062(28)	0.00(3)	0.77(5)
377	0.46(3)	< 0.02	0.05(5)	0.03(4)		0.32(6)	0.11(5)	0.03(6)	< 0.01	0.77(8)
300	0.44(4)		0.06(5)	0.06(6)		0.37(8)	0.07(6)			0.77(11)
258	0.49(3)			0.14(4)		0.37(5)				0.76(7)

est energy point at $E_{\mathrm{c.m.}} = 470\,\mathrm{keV}$, the fitted widths of the other three energy points were averaged, and this width was used to fit the distribution at $E_{\mathrm{c.m.}} = 470\,\mathrm{keV}$. The averaged width of the distributions (0.81(2)) was found to be in agreement with the value calculated according to Ref. [17] (0.79). The average charge state values $\bar{q}$ of the distributions are compared to the calculated values in Table V. At $E_{\mathrm{c.m.}} = 300\,\mathrm{keV}$, the calculated $\bar{q}$ is

TABLE V. Center of charge state distributions $\bar{q}$, comparison of fitted and calculated ([17]) values.

	$\bar{q}$	
$E_{\mathrm{c.m.}}$ [keV]	fitted	calculated
470	5.52 ± 0.02	5.39
377	4.84 ± 0.03	4.84
300	4.13 ± 0.04	4.25
258	3.80 ± 0.03	3.86

slightly large, at $E_{\mathrm{c.m.}} = 470\,\mathrm{keV}$ it is slightly small, for the other two energies the values agree. This confirms the validity of the parameters derived in Ref. [17] for ^{18}F at these energies, which were calculated assuming that the charge state distribution has reached equilibrium at the end of the target. Based on the comparison, the reaction products appear to have reached equilibrium.

D. Astrophysical S factor

Using the fitted Gaussian distributions, the contributions from the unmeasured charge states were calculated and added to the measured values to give the total S factor. The results are given in Table VI. Figure 9 shows the

TABLE VI. Total S factor, including contributions from unmeasured charge states. The statistical and systematic uncertainties are given separately.

$E_{\mathrm{c.m.}}$ [keV]	S factor [keVb]
470	$21.0 \pm 0.3 \pm 2.7$
377	$12.0 \pm 0.4 \pm 1.9$
300	$7.9 \pm 0.5 \pm 1.6$
258	$6.9 \pm 0.2 \pm 1.1$

S factor values determined in this work as well as those

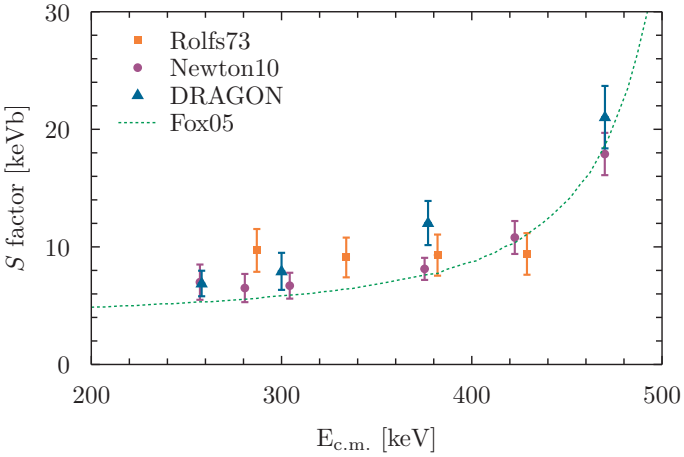

FIG. 9. (color online) S factor, comparison to literature [4, 7, 8]

measured by Rolfs [7] and Newton *et al.* [8]. Our results clearly show the S factor decreasing with decreasing energy, in contrast to [7], where the S factor was found to be constant with energy. For the three highest energies, our values lie above those given by Newton *et al.* [8], though the discrepancy is less than 1σ except for the values at $E_{\mathrm{c.m.}} = 375\,\mathrm{keV}$, which differ by about 2.2σ. Their lower values might be due to an unobserved γ line or problems with the background in Ref. [8]. Our values are also consistently higher than the evaluation by Fox *et al.* [4]. However, at lower energies, their values lie below all experimental values. Comparing the shape of the calculated curve presented by Fox *et al.* to the energy dependence of the S factor presented in this work, it seems likely that the width or strength of the $E_{\mathrm{c.m.}} = 557\,\mathrm{keV}$ or $E_{\mathrm{c.m.}} = 677\,\mathrm{keV}$ resonances used in Ref. [4] are too low and need to be re-investigated in future experiments.

IV. SUMMARY

We presented a direct measurement of the $^{17}\mathrm{O}(p,\gamma)^{18}\mathrm{F}$ reaction rate in the energy range $E_{\mathrm{c.m.}} = 250 - 500\,\mathrm{keV}$. Our measured S factors are higher than those presented in Ref. [8] and in Ref. [4]. The flat energy dependence of the S factor found in Ref. [7] could not be confirmed. Astrophysical conclusions cannot at this point be

reached. The disagreement with the rate presented in [4] calls for a re-evaluation of the contributions from higher resonances. Additionally, conflicting information exists also on the $E_{\mathrm{c.m.}} = 183\,\mathrm{keV}$ resonance [2, 18]. Measurements of the resonances are required to re-evaluate their influence on the reaction strength in this energy range, and to determine the DC contribution to the total reaction rate.

ACKNOWLEDGMENTS

We would like to thank the beam delivery and ISAC operations groups at TRIUMF. The authors gratefully acknowledge funding from the Natural Sciences and Engineering Research Council of Canada. The Colorado School of Mines group was funded via grant DE-FG02-93ER40789 from the U.S. Department of Energy, Office of Nuclear Physics. We also gratefully acknowledge the invaluable assistance in beam production from K. Jayamanna.

[1] A. Coc, M. Hernanz, J. José, and J.-P. Thibaud, Astron. Astrophys **357**, 561 (2000).
[2] A. Chafa, V. Tatischeff, P. Aguer, S. Barhoumi, A. Coc, F. Garrido, M. Hernanz, J. José, J. Kiener, A. Lefebvre-Schuhl, et al., Phys. Rev. C **75**, 035810 (2007), URL http://link.aps.org/doi/10.1103/PhysRevC.75.035810.
[3] C. E. Rolfs and W. S. Rodney, *Cauldrons in the Cosmos* (The University of Chicago Press, 1988).
[4] C. Fox, C. Iliadis, A. E. Champagne, R. P. Fitzgerald, R. Longland, J. Newton, J. Pollanen, and R. Runkle, Phys. Rev. C **71**, 055801 (2005), URL http://link.aps.org/doi/10.1103/PhysRevC.71.055801.
[5] J. José and M. Hernanz, Astrophys. J. **494**, 680 (1998).
[6] C. Iliadis, A. Champagne, J. José, S. Starrfield, and P. Tupper, Astrophys. J. Suppl. **142**, 105 (2002).
[7] C. Rolfs, Nucl. Phys. A **217**, 29 (1973).
[8] J. R. Newton, C. Iliadis, A. E. Champagne, J. M. Cesaratto, S. Daigle, and R. Longland, Phys. Rev. C **81**, 045801 (2010).
[9] D. A. Hutcheon, S. Bishop, L. Buchmann, M. L. Chatterjee, A. A. Chen, J. M. D'Auria, S. Engel, D. Gigliotti, U. Greife, D. Hunter, et al., Nucl. Instr. Meth. A **498**, 190 (2003).
[10] K. Jayamanna, Rev. Sci. Instrum. **81**, 02A331 (2010).
[11] J. M. D'Auria, R. E. Azuma, S. Bishop, L. Buchmann, M. L. Chatterjee, A. A. Chen, S. Engel, D. Gigliotti, U. Greife, D. Hunter, et al., Phys. Rev. C **69**, 065803 (2004).
[12] C. Vockenhuber, L. Buchmann, J. Caggiano, A. Chen, J. D'Auria, C. Davis, U. Greife, A. Hussein, D. Hutcheon, D. Ottewell, et al., Nucl. Instr. Meth. B **266**, 4167 (2008).
[13] C. Vockenhuber, L. Erikson, L. Buchmann, U. Greife, U. Hager, D. Hutcheon, M. Lamey, P. Machule, D. Ottewell, C. Ruiz, et al., Nucl. Instr. Meth. A **603**, 372 (2009).
[14] D. Hutcheon, L. Buchmann, A. Chen, J. DAuria, C. Davis, U. Greife, A. Hussein, D. Ottewell, C. Ouellet, A. Parikh, et al., Nucl. Instr. Meth. B **266**, 4171 (2008), ISSN 0168-583X, URL http://www.sciencedirect.com/science/article/pii/S0168583X0800699X.
[15] D. G. Gigliotti, J. G. Rogers, and A. H. Hussein, Nucl. Instr. Meth. B **204**, 671 (2003).
[16] D. Tilley, H. Weller, C. Cheves, and R. Chasteler, Nucl. Phys. A **595**, 1 (1995), ISSN 0375-9474, URL http://www.sciencedirect.com/science/article/pii/0375947495003381.
[17] W. Liu, G. Imbriani, L. Buchmann, A. Chen, J. DAuria, A. DOnofrio, S. Engel, L. Gialanella, U. Greife, D. Hunter, et al., Nucl. Instr. Meth. A **496**, 198 (2003), ISSN 0168-9002, URL http://www.sciencedirect.com/science/article/pii/S0168900202016297.
[18] C. Fox et al., Phys. Rev. Lett. **93**, 081102 (2004).